Nonlinear bending of unsymmetric double-layer lattice truss core sandwich beams

Na Hao[a], Linfeng Zhu[a,*], Zhangming Wu[b,c], Liaoliang Ke[a,*]

[a] *School of Mechanical Engineering, Tianjin University, Tianjin, 300350, China*

[b] *School of Mechanical Engineering and Mechanics, Ningbo University, Ningbo, 315211, China*

[c] *School of Engineering, Cardiff University, Cardiff CF24 3AA, UK*

Abstract

This paper endeavors to study the nonlinear bending of unsymmetric double-layer lattice truss core sandwich beams (LTCSBs). Five unsymmetric cases of the double-layer LTCSBs are considered by varying different materials and geometric thicknesses in two layers. To establish a theoretical model for the unsymmetric double-layer LTCSBs, Allen's model and von Kármán nonlinear theory are employed. The present theoretical model for the double-layer LTCSBs is established by considering the midplane of the mid-sheet as the reference plane. A theoretical model based on the Ritz method is applied to determine the deflection for the nonlinear bending of the unsymmetric double-layer LTCSBs, and verified by the finite element method (FEM). Finally, the effects of the loading direction, unsymmetric factors in material property and structural geometry, and boundary conditions on the nonlinear bending behaviors of LTCSBs are studied. This study reveals that, under certain boundary conditions, the nonlinear deflections of unsymmetric LTCSBs will become different when the loading with the same magnitude applied from different directions, and sometimes may exhibit softening-spring nonlinearity in one direction.

Keywords: Softening-spring nonlinearity, Sandwich beams, Nonlinear bending, Lattice truss core

*Corresponding author: Liao-Liang Ke; E-mail: llke@tju.edu.cn
Lin-Feng Zhu; E-mail: lfzhu@tju.edu.cn

1. Introduction

A typical lattice structure is comprised of two stiff face sheets and a lightweight sandwich core between them to achieve high strength yet light weight (Li et al. 2022; Yang et al. 2020). The core often possesses high porosity and is available in different typologies such as pyramidal, Kagome, tetrahedral, and hourglass (Lou et al. 2013; Xu and Qiu 2013; Zhao, Wen and Li 2018; Guo et al. 2021). The porosity of sandwich cores makes it possible to embed electric components enabling the lattice structures to achieve functions of absorbing energy, reducing noise, and shielding electromagnetic radiation (Nasrullah, Santosa, and Dirgantara 2020; Wadley et al. 2008; Evans et al. 2001). These prominent advantages and multifunctional applications make the lattice structures become one of most promising materials in engineering applications (Vinson 2005).

The structural geometry and material property of the lattice truss core in sandwich structures play a key role on their mechanical properties, making them a subject of interest among many researchers who aim to design and manufacture novel lightweight structures for various engineering applications. For instance, Zhang et al. (2018) designed the shapes of free-form truss in Kagome lattice cores by optimizing the critical buckling loads of sandwich panels, achieving 20.4% improvement of the critical buckling load for an optimized 3D structure compared to a uniform Kagome lattice core sandwich structure with the same mass. Xu et al. (2016) proposed a new method to fabricate graded corrugated truss core sandwich structures and found that the graded form can significantly affect the bending behavior and failure mode of structures. Yin et al. (2011) fabricated sandwich structures with hollow composite pyramidal lattice trusses using a thermal expansion molding technique. Li et al. (2020) devised a multilayer lattice sandwich beam and studied its vibrational characteristics. Yang et al. (2021) designed sandwich panels with a multilayer gradient lattice core, demonstrating that the multilayer gradient lattice sandwich structure possessed higher impact strength and better energy abortion ability than that of non-gradient structures. Ni et al. (2017) discussed the ballistic protection performance of a double-layer metallic pyramidal lattice truss core sandwich structure filled with ceramic prisms and epoxy resin. Wang et al. (2022) studied the compressive properties and failure mechanisms of hierarchical lattice structures at high temperature through both experimental and numerical methods.

In recent years, there has been increasing concerns regarding vibration, bending, and buckling problems in many engineering fields (Xiong et al. 2014; Yuan et al. 2016; Fan, Meng and Yang 2006; Lou, Ma and Wu 2012; Li et al. 2022). Chai et al. (2021) investigated the vibration characteristics of single-

layer pyramidal lattice sandwich plates using theoretical, experimental, and numerical methods. Zhang et al. (2020) presented a study on the bending behavior of pyramidal lattice core sandwich panels, in which they constructed the failure mechanism maps by analyzing the critical load of face sheet crashing, core member crashing, core shear failure, and interlayer delamination. Xiong et al. (2011) studied the axial compression of composite pyramidal truss core sandwich structure considering three failure modes, e.g., Euler buckling, face wrinkling, and face crushing. Chen et al. (2013) investigated the thermal buckling of truss-core sandwich plates using an equivalent homogeneous method. Li et al. (2016) developed a solid-element method based on the layerwise theory to analyze the static response and free vibration of multi-layer core sandwich structure. Cao et al. (2017) investigated the out-of-plane compression behaviour of multilayered corrugated core sandwiches using numerical and experimental methods.

Previous research works mainly focused on the linear behavior for the lattice truss core sandwich structures. However, it is crucial to deeply understand the nonlinear performance of these structures servicing in severe conditions. Nampally et al. (2019) investigated the global nonlinear bending of two-dimensional (2D) sandwich beams with different lattice cores using both theoretical and numerical methods. Zhang et al. (2022) examined the nonlinear vibration responses of lattice truss sandwich beams with functionally graded material face sheets using an improved equivalent methodology. Chai et al. (2019) analyzed the nonlinear flutter and thermal buckling of tetrahedral lattice truss core sandwich panel based on the assumed mode method. Further, Chai et al. (2019) investigated the nonlinear vibration, bifurcations, and chaos behaviors of lattice sandwich composite panels resting on Winkler-Pasternak elastic foundations.

It is important to note that the above research works primarily focused on the nonlinear behaviors of single-layer sandwich structures. However, there has been limited research to study the nonlinear behaviour of double-layer and multi-layer lattice truss core sandwich structures, or single-layer sandwich structures with multi-layer cores. Li et al. (2020) conducted both numerical and experimental studies into the nonlinear bending behaviors of the sandwich structure with multi-layer 3D auxetic lattice cores. Their findings revealed that the auxetic core remarkably reduced the lateral deflections compared to non-auxetic counterparts. Li et al. (2020) examined the nonlinear vibration of sandwich plates with multi-layer auxetic 3D lattice cores using experiments and full-scale nonlinear finite element simulations. Hao et al. (2023) investigated the nonlinear vibration of the unsymmetric double-layer lattice truss core sandwich beams, where they discovered the softening-spring nonlinearity phenomenon under certain boundary conditions.

The present study investigates the global nonlinear bending behavior of the unsymmetric double-layer

lattice truss core sandwich beams (LTCBs) using Ritz method and finite element method (FEM). Five unsymmetric cases of double-layer LTCSBs possessing different materials or geometric thicknesses in two layers are considered. A theoretical model for LTCSBs is established based on Allen's model and von Kármán nonlinearity. The Ritz method is applied to determine the nonlinear deflections of double-layer LTCSBs. A parametric study is performed to discuss the effects of boundary conditions and loading directions on the nonlinear bending of double-layer LTCBs with five different unsymmetric cases.

2. Unsymmetric double-layer LTCSB

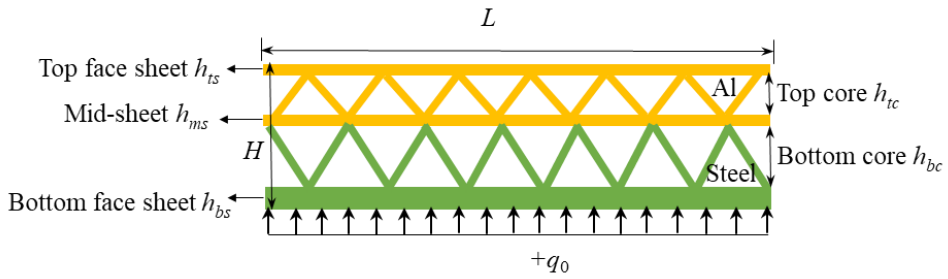

Figure 1. Sketch of the unsymmetric double-layer LTCSB subjected to the uniformly distributed load.

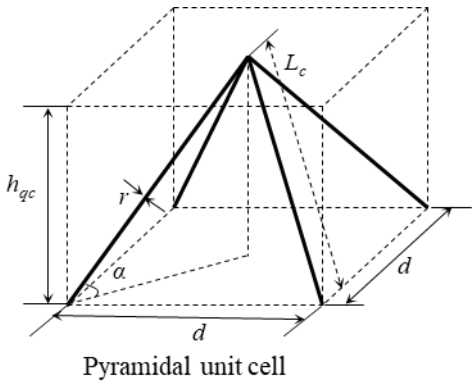

Figure 2. The unit cell in the top and bottom core layers.

Fig. 1 shows the unsymmetric model of a double-layer LTCSB subjected to uniformly distributed load on the bottom face sheet. The structure comprises three face sheets and two cores with varying materials and geometric thicknesses along the transverse direction. h_{es} and h_{qc} represent the thicknesses of the face sheets and cores, respectively, where the subscripts $q = t,\ b$ and $e = t,\ b,\ m$. The subscripts s and c denote 'sheet' and 'core', and the subscripts t, m, and b, represent 'top', 'middle', and 'bottom', respectively. The total length and thickness of the beam are L and H ($H = h_{ts} + h_{tc} + h_{ms} + h_{bc} + h_{bs}$). Fig.

2 illustrates the pyramidal unit cell in the two core layers, where the unit cell width is d . The inclination angle, length, and radius of the struts are denoted by α , L_c , and r , respectively. Note that the signs "+" and "–" of q_0 indicate the directions of the external load. In other words, $+q_0$ represents the load that is exerted on the bottom face sheet, while $-q_0$ indicates that the load is exerted on the top face sheet.

In this study, five unsymmetric cases are considered as follows:

Case I: The structural unsymmetry arises from the differences of material properties in sheets and cores. The materials of the bottom sheet and bottom core are steel, and the material of the rest part is aluminum (Al).

Case II: The structural unsymmetry is due to the thickness of top sheet is different from that of bottom sheet (h_{ts} and h_{bs}). The whole structure is made of Al.

Case III: The unsymmetric nature of the structure is due to the thickness of the top core that is different with that of bottom core (h_{tc} and h_{bc}). The whole structure is made of Al.

Case IV: The unsymmetric nature of the structure arises from the combination of material property and structural geometry of sheets (Case I + Case II).

Case V: The unsymmetric nature of the structure is due to the combination of material property and structural geometry of cores (Case I + Case III).

When analyzing the global behaviour of lattice truss core sandwich structures, it is a common practice to substitute the lattice truss core with a continuum layer (Liu, Xiang and Kan 2015). The relative density and equivalent shear modulus of pyramidal truss core are described in Liu et al. (2021)

$$\bar{\rho} = \frac{2\pi r^2}{L_c^{\,2}\cos^2(\alpha)\sin(\alpha)}, \tag{1}$$

$$G_c = \frac{E_0 \cdot \bar{\rho} \cdot \sin^2(2\alpha)}{8}, \tag{2}$$

where α is the inclination angle of the struts, and E_0 represents the elastic modulus of the unit cell material.

3. The mathematical model and solution process

In the theory analysis of sandwich structures, Allen's model is applied. Allen's model was specially proposed for the sandwich structure composed of face sheets and cores. Compared with the incline line form for axial displacement of Timoshenko beam theory and Euler-Bernoulli beam theory, Allen's model

introduces the broken line form for the axial displacement (Allen 1969; Meng et al. 2020). It describes the characteristics well for the sandwich structures whose face sheets are rigid and cores are soft. In the Allen's model, the face sheet is assumed as an Euler beam, and only transverse shear deformation is considered for the core.

Fig. 3 illustrates the infinitesimal deformation for an equivalent model of the unsymmetric double-layer LTCSB for the present model and our previous model (Hao et al. 2023). In our previous paper, we studied the nonlinear vibration of the unsymmetric double-layer LTCSBs where the reference plane was the geometric mid-plane of the whole structure as shown in Fig. 3(a). Due to the difference of rotation angles between the face sheet and core, the displacement field for the five cases need to be divided two situations according to the location of reference plane: (i) the reference plane locates at the mid-sheet for the unsymmetric material property (structure geometry is symmetric), and (ii) the reference plane locates on the bottom core for the unsymmetric structure geometry. However, the reference plane is fixed on the midplane of mid-sheet in present model as shown in Fig. 3(b). The reason for using the mid-plane of mid-sheet as the reference plane is because the displacement formulations for the five cases can be unified.

In Fig. 3(b), the displacement field of unsymmetric double-layer LTCSBs is established with respect to the mid-plane of the mid-sheet in the present model. According to Allen's broken line model, the transverse displacements of sheets and cores are the same, but their axial displacements, as well as rotation angles, differ. Therefore, the axial displacements of different layers for the five cases are given as (Lou et al. 2013; Meng et al. 2020)

$$u_{ts} = u\left(x,t\right) - h_{tc}\theta - \left(z - h_{tc}\right)\frac{\partial w}{\partial x},\ \frac{h_{ms}}{2} + h_{tc} \le z \le \frac{h_{ms}}{2} + h_{tc} + h_{ts}, \tag{3}$$

$$u_{tc} = u\left(x,t\right) - \frac{h_{ms}}{2}\frac{\partial w}{\partial x} - \left(z - \frac{h_{ms}}{2}\right)\theta,\ \frac{h_{ms}}{2} \le z \le \frac{h_{ms}}{2} + h_{tc}, \tag{4}$$

$$u_{ms} = u\left(x,t\right) - z\frac{\partial w}{\partial x},\ -\frac{h_{ms}}{2} \le z \le \frac{h_{ms}}{2}, \tag{5}$$

$$u_{bc} = u\left(x,t\right) + \frac{h_{ms}}{2}\frac{\partial w}{\partial x} - (z + \frac{h_{ms}}{2})\theta,\quad -\frac{h_{ms}}{2} - h_{bc} \le z \le -\frac{h_{ms}}{2}, \tag{6}$$

$$u_{bs} = u\left(x,t\right) + h_{bc}\theta - \left(z + h_{bc}\right)\frac{\partial w}{\partial x},\ -\frac{h_{ms}}{2} - h_{bc} - h_{ts} \le z \le -\frac{h_{ms}}{2} - h_{bc}, \tag{7}$$

where u and w are the displacement components in the mid-plane of the mid-sheet; θ represents the rotation angle of core layers and $\partial w/\partial x$ is the rotation of face sheets. u_{es} and u_{qc} are the axial displacements of face sheets and core layers, respectively.

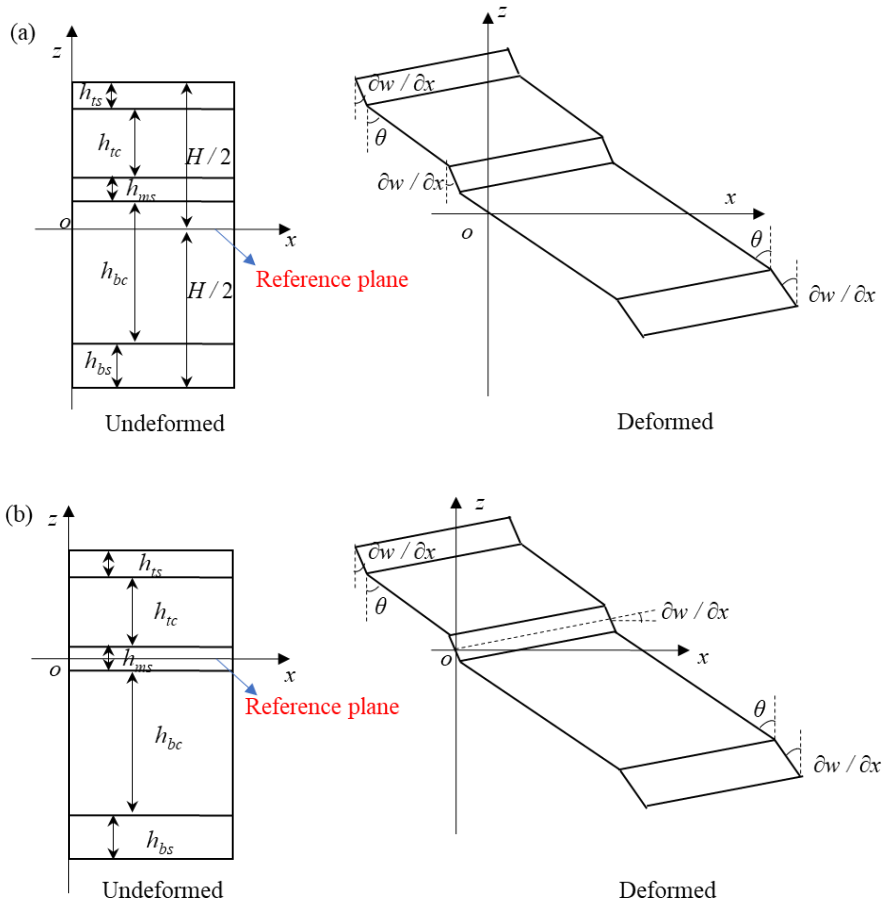

Figure 3. Deformation of equivalent model of the unsymmetric double-layer LTCSBs in *xz*-plane based on Allen's model: (a) previous model by Hao et al. (2023), (b) present model.

With the von Kármán nonlinear geometric relationship, the strains of three face sheets and two core layers are expressed as

$$\varepsilon_{es} = \frac{\partial u_{es}}{\partial x} + \frac{1}{2}\left(\frac{\partial w}{\partial x}\right)^2, \tag{8}$$

$$\gamma_{qc} = \frac{\partial w}{\partial x} - \theta, \tag{9}$$

where ε_{es} denotes the normal strain of the sheet, and γ_{qc} denotes the shear strain of the core layer.

Based on the linear elastic constitutive law, the normal stresses of face sheets and the shear stresses of cores are expressed as

$$\sigma_{es} = E_{es}\varepsilon_{es}, \ \tau_{qc} = G_{qc}\gamma_{qc}. \tag{10}$$

The corresponding normal stresses σ_{ts}, σ_{ms}, σ_{bs}, and shear stresses τ_{tc}, τ_{bc} are expressed in terms of displacements according to Eqs. (8) - (10). The axial force and bending moment of the beam are given by,

$$N_x = B\left(\int \sigma_{ts}\mathrm{d}z + \int \sigma_{ms}\mathrm{d}z + \int \sigma_{bs}\mathrm{d}z\right), \tag{11}$$

$$M_x = B\left(\int z\sigma_{ts}\mathrm{d}z + \int z\sigma_{ms}\mathrm{d}z + \int z\sigma_{bs}\mathrm{d}z\right), \tag{12}$$

where B denotes the beam width.

The strain energy Q is expressed as Kitipornchai et al. (2009)

$$Q = \frac{B}{2}\int_0^L \left\{ \int_{\frac{h_{ms}}{2}+h_{tc}}^{\frac{h_{ms}}{2}+h_{tc}+h_{ts}} \sigma_{ts}\varepsilon_{ts}\mathrm{d}z + \int_{\frac{h_{ms}}{2}}^{\frac{h_{ms}}{2}+h_{tc}} \tau_{tc}\gamma_{tc}\mathrm{d}z + \int_{-\frac{h_{ms}}{2}}^{\frac{h_{ms}}{2}} \sigma_{ms}\varepsilon_{ms}\mathrm{d}z + \int_{-\frac{h_{ms}}{2}-h_{bc}}^{-\frac{h_{ms}}{2}} \tau_{bc}\gamma_{bc}\mathrm{d}z + \int_{-\frac{h_{ms}}{2}-h_{bc}-h_{bs}}^{-\frac{h_{ms}}{2}-h_{bc}} \sigma_{bs}\varepsilon_{bs}\mathrm{d}z \right\}\mathrm{d}x. \tag{13}$$

From Eqs. (1) - (13), the potential energy Q ($Q = Q_{linear} + Q_{nonlinear}$), axial force, and bending moment are expressed as follows,

$$\begin{aligned} Q_{linear} = \frac{B}{2}\int_0^L \Bigg\{ & A_{11}\left(\frac{\partial u}{\partial x}\right)^2 + A_{13}\left(\frac{\partial \theta}{\partial x}\right)^2 + \left(D_{11} + A_{13} - 2B_{12}\right)\left(\frac{\partial^2 w}{\partial x^2}\right)^2 - 2A_{12}\frac{\partial u}{\partial x}\frac{\partial \theta}{\partial x} \\ & - 2\left(B_{11} - A_{12}\right)\frac{\partial u}{\partial x}\frac{\partial^2 w}{\partial x^2} + A_{00}\left[\left(\frac{\partial w}{\partial x}\right)^2 - 2\theta\frac{\partial w}{\partial x} + \theta^2\right] + 2\left(B_{12} - A_{13}\right)\frac{\partial \theta}{\partial x}\frac{\partial^2 w}{\partial x^2}\Bigg\}\mathrm{d}x \end{aligned}, \tag{14}$$

$$Q_{nonlinear} = \frac{B}{2}\int_0^L \left\{ \frac{A_{11}}{4}\left(\frac{\partial w}{\partial x}\right)^4 + A_{11}\frac{\partial u}{\partial x}\left(\frac{\partial w}{\partial x}\right)^2 - A_{12}\frac{\partial \theta}{\partial x}\left(\frac{\partial w}{\partial x}\right)^2 - \left(B_{11} - A_{12}\right)\left(\frac{\partial w}{\partial x}\right)^2\frac{\partial^2 w}{\partial x^2}\right\}\mathrm{d}x, \tag{15}$$

$$N_x = A_{11}\left[\frac{\partial u}{\partial x} + \frac{1}{2}\left(\frac{\partial w}{\partial x}\right)^2\right] - A_{12}\frac{\partial \theta}{\partial x} + \left(A_{12} - B_{11}\right)\frac{\partial^2 w}{\partial x^2}, \tag{16}$$

$$M_x = B_{11}\left[\frac{\partial u}{\partial x} + \frac{1}{2}\left(\frac{\partial w}{\partial x}\right)^2\right] - B_{12}\frac{\partial \theta}{\partial x} + \left(B_{12} - D_{11}\right)\frac{\partial^2 w}{\partial x^2}, \tag{17}$$

where

$$A_{00} = S_{tc} + S_{bc},\ A_{11} = A_{ts} + A_{ms} + A_{bs},\ A_{12} = h_{tc}A_{ts} - h_{bc}A_{bs},$$

$\mathrm{A}_{13} = {h_{tc}}^2 A_{ts} + {h_{bc}}^2 A_{bs}$, $B_{11} = B_{ts} + B_{ms} + B_{bs}$, $B_{12} = h_{tc}B_{ts} - h_{bc}B_{bs}$, $D_{11} = D_{ts} + D_{ms} + D_{bs}$. Note that the total energy Q is divided linear part Q_{linear} and nonlinear part $Q_{nonlinear}$ according to the linear strain and nonlinear term in Eq. (8) for the convenience. The unknown terms in A_{00}, A_{11}, A_{12}, A_{13}, B_{11}, B_{12}, and D_{11} are expressed as Chen et al. (2016)

$$\begin{aligned} & \left(A_{ts}, B_{ts}, D_{ts}\right) = \int_{\frac{h_{ms}}{2}+h_{tc}}^{\frac{h_{ms}}{2}+h_{tc}+h_{ts}} E_{ts}\left(1, z, z^2\right)\mathrm{d}z,\ \left(A_{ms}, B_{ms}, D_{ms}\right) = \int_{-\frac{h_{ms}}{2}}^{\frac{h_{ms}}{2}} E_{ms}\left(1, z, z^2\right)\mathrm{d}z, \\ & \left(A_{bs}, B_{bs}, D_{bs}\right) = \int_{-\frac{h_{ms}}{2}-h_{bc}-h_{bs}}^{-\frac{h_{ms}}{2}-h_{bc}} E_{bs}\left(1, z, z^2\right)\mathrm{d}z,\ S_{tc} = \int_{\frac{h_{ms}}{2}}^{\frac{h_{ms}}{2}+h_{tc}} G_{tc}\mathrm{d}z, S_{bc} = \int_{-\frac{h_{ms}}{2}-h_{bc}}^{-\frac{h_{ms}}{2}} G_{bc}\mathrm{d}z. \end{aligned} \tag{18}$$

The bending-extension coupling effect arises from the unsymmetry of material properties or structural

geometry along the transverse direction, which then causes the non-coincidence of the reference plane and neutral plane of the double-layer LTCSBs (Hao et al. 2023). The coefficient B_{11} plays an important role in the bending-extension coupling effect. The work J done by the uniform load q_0 is given by

$$J = B\int_0^L q_0 w \mathrm{d}x. \tag{19}$$

The following transformations of variables and parameters are introduced to obtain dimensionless equations,

$$\begin{aligned}
&\xi = \frac{x}{L},\ (U,W) = \frac{(u,w)}{H},\ \varphi = \theta,\ A_{10} = \int_{-\frac{h_{ms}}{2}-h_{bc}-h_{bs}}^{\frac{h_{ms}}{2}+h_{tc}+h_{ts}} E_{bs}\mathrm{d}z,\ \ \zeta_1 = \frac{h_{bc}}{H},\\
&\zeta_2 = \frac{H}{L}, \zeta_3 = \frac{h_{tc}}{H},\ \left(\bar{A}_{es}, \bar{B}_{es}, \bar{D}_{es}\right) = \frac{\left(A_{es}, B_{es}, D_{es}\right)}{A_{10}\left(1, H, H^2\right)},\ \bar{S}_{qc} = \frac{S_{qc}}{A_{10}}, N_x^{\ *} = \frac{N_x}{A_{10}},\\
&Q^*_{\ linear} = \frac{Q_{linear}}{\Delta_0},\ Q^*_{\ nonlinear} = \frac{Q_{nonlinear}}{\Delta_0},\ q_0^* = \frac{q_0 L^2}{A_{10}H},\ J^* = \frac{J}{\Delta_0}, \Delta_0 = \frac{BA_{10}H^2}{L}.
\end{aligned} \tag{20}$$

Substituting Eq. (20) into Eqs. (14), (15), and (19), the total energy of the unsymmetric double-layer LTCSBs is expressed in the following dimensionless form as,

$$\Pi = Q^*_{\ linear} + Q^*_{\ nonlinear} - J^*. \tag{21}$$

The dimensionless form of axial force is

$$N_x^{\ *} = \bar{A}_{11}\left[\zeta_2 \frac{\partial U}{\partial \xi} + \frac{1}{2}\zeta_2^{\ 2}\left(\frac{\partial W}{\partial \xi}\right)^2\right] - \bar{A}_{12}\zeta_2 \frac{\partial \varphi}{\partial \xi} + \left(\bar{A}_{12} - \bar{B}_{11}\right)\zeta_2^{\ 2}\frac{\partial^2 W}{\partial \xi^2}, \tag{22}$$

where $\bar{A}_{11}$, $\bar{A}_{12}$, and $\bar{B}_{11}$ are the dimensionless forms of A_{11}, A_{12}, and B_{11}.

The Ritz trial functions of the different boundary conditions including hinged-hinged (H–H), clamped-clamped (C–C), and clamped-hinged (C–H) are given as Ke et al. (2010):

H–H:
$$\begin{cases} U(\xi) = \sum_{j=1}^{N} A_j \xi^j (1-\xi), \\ W(\xi) = \sum_{j=1}^{N} B_j \xi^j (1-\xi), \\ \varphi(\xi) = \sum_{j=1}^{N} C_j \xi^{j-1}, \end{cases} \tag{23}$$

C–C:
$$\begin{cases} U(\xi) = \sum_{j=1}^{N} A_j \xi^j (1-\xi), \\ W(\xi) = \sum_{j=1}^{N} B_j \xi^j (1-\xi), \\ \varphi(\xi) = \sum_{j=1}^{N} C_j \xi^j (1-\xi), \end{cases} \tag{24}$$

C–H:

$$\begin{cases} U(\xi)=\sum_{j=1}^{N} A_j \xi^j (1-\xi), \\ W(\xi)=\sum_{j=1}^{N} B_j \xi^j (1-\xi), \\ \varphi(\xi)=\sum_{j=1}^{N} C_j \xi^j, \end{cases} \tag{25}$$

in which N represents the number of polynomial terms; A_j, B_j, and C_j denote unknown coefficients of polynomial terms. Substituting one of boundary conditions into the dimensionless form of total energy function, and applying a standard Ritz procedure, a set of nonlinear algebraic equations are derived (Liew et al. 1998), as follows:

$$\frac{\partial \Pi}{\partial A_j}=0,\ \frac{\partial \Pi}{\partial B_j}=0,\ \frac{\partial \Pi}{\partial C_j}=0. \tag{26}$$

Finally, the nonlinear bending problem is expressed in a matrix form as

$$\left(\left[\mathbf{K}_{\mathbf{L}}\right]+\left[\mathbf{K}_{\mathbf{NL1}}\right]+\left[\mathbf{K}_{\mathbf{NL2}}\right]\right)\mathbf{d}=\mathbf{V}_{\mathbf{q}}, \tag{27}$$

where $\mathbf{d}=\{\{A_j\}^{\mathrm{T}},\{B_j\}^{\mathrm{T}},\{C_j\}^{\mathrm{T}}\}$, $j=1,2,...,N$; $\mathbf{V}_{\mathbf{q}}=\left\{\{0\}^{\mathrm{T}},\{\boldsymbol{q}_0\}^{\mathrm{T}},\{0\}^{\mathrm{T}}\right\}$ is the vector associated with the external load, $\left[\mathbf{K}_{\mathbf{L}}\right]$, $\left[\mathbf{K}_{\mathbf{NL1}}\right]$, and $\left[\mathbf{K}_{\mathbf{NL2}}\right]$ are the linear stiffness matrix and nonlinear stiffness matrices, respectively. $\left[\mathbf{K}_{\mathbf{NL1}}\right]$ is a linear function of $\mathbf{d}$ while $\left[\mathbf{K}_{\mathbf{NL2}}\right]$ is a quadratic function of $\mathbf{d}$.

After ignoring the nonlinear terms in Eq. (27), the linear bending problem of unsymmetric double-layer LTCSB is reduced into the following matrix form,

$$\left[\mathbf{K}_{\mathbf{L}}\right]\mathbf{d}=\mathbf{V}_{\mathbf{q}}. \tag{28}$$

An iterative procedure is required to solve this nonlinear bending problem given by Eq. (27). The linear algebraic equation (28) needs to be solved first to obtain initial values for the iterative procedure. The specific steps are described as follows (Anirudh et al. 2020),

1. Solve the linear equation Eq. (28) for a given $+q_0^*$ or $-q_0^*$, and obtain the linear deflection W_0.

2. Substitute the linear deflection W_0 into the nonlinear stiffness matrices $\left[\mathbf{K}_{\mathbf{NL1}}\right]$ and $\left[\mathbf{K}_{\mathbf{NL2}}\right]$, the new unknown coefficients $\mathbf{d}=\{\{A_j\}^{\mathrm{T}},\{B_j\}^{\mathrm{T}},\{C_j\}^{\mathrm{T}}\}$ are updated from Eq. (27) to obtain new deflection W.

3. Repeat steps 1 and 2 until the relative error of the maximum deflection in two consecutive iterations is less than 0.01%.

All elements in stiffness matrices and corresponding coefficients in dimensionless forms are given in

Appendix A.

4. Finite element simulation

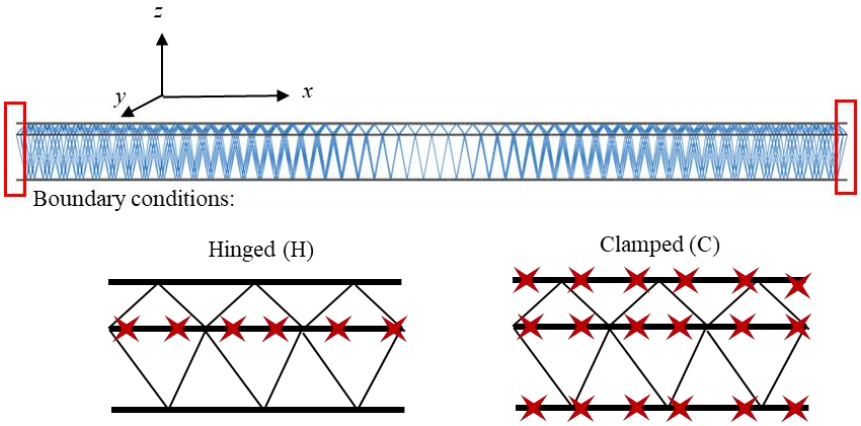

Figure 4. Finite element model and different boundary conditions of the double-layer LTCSB for case III.

The Finite element method (FEM) is used to verify the prediction accuracy of the theorical model on the linear and nonlinear bending deflections under different boundary conditions. The FEM model for case III double-layer LTCSB is established using Abaqus software, as shown in Fig. 4. This double-layer beam consists of $50\times3\times2$ unit cells in total, which is generated by repeating the top and bottom unit cells 50 times and 3 times along the x and y directions, respectively. The cells of the double-layer LTCSB are assembled by merging operations. The C–C, C–H, and H–H boundary conditions are considered in the FEM analysis, and the displacements field of y-direction ($U2$) is restricted to be zero to make the 3D finite element model close to the 2D theorical model (Radice 2012). The clamped (C) boundary condition exerted on the three sheets' ends is expressed as $U1=U2=U3=UR1=UR2=UR3=0$ where $U1$, $U2$, $U3$, $UR1$, $UR2$, and $UR3$ are the displacement degrees of freedom and rotational displacement degrees of freedom along the x-, y-, z-directions, respectively. The hinged (H) boundary condition is constrained on the ends of mid-sheet with $U1=U2=U3=0$ (Radice 2012).

In the FEM model, a combination of shell element (S4) and beam element (B32) is used for three sheets and all struts in two core layers, respectively. Mesh convergence is achieved with 10 elements for each strut and 20 elements for the side of each unit sheet. A uniform load is applied on the top or bottom face sheet of the double-layer LTCSB. Note, the Nlgeom option is switched on for the nonlinear bending analysis with geometric large deformations.

5. Results and discussions

This paper aims to study the nonlinear bending behavior of unsymmetric double-layer LTCSBs subjected to uniform loading q_0 , which may be applied from different directions. Five different unsymmetric cases of double-layer LTCSBs are considered. In cases I–III, a single unsymmetric factor is considered, e.g., either on material or structure geometry, whereas cases IV and V consider a combination of both factors. Table 1 lists the specific geometry parameters of the five cases of unsymmetric double-layer LTCSBs. The material properties of steel and aluminum are: $E_{\text{steel}} = 210$ GPa, $\nu_{\text{steel}} = 0.3$, $E_{\text{Al}} = 70$ GPa , and $\nu_{\text{Al}} = 0.33$.

Table 1. Geometry parameters of double-layer LTCSBs in different cases (L=106.07 cm and B=6.36 cm).

Parameters	Cases I	Case II	Case III	Case IV	Case V
h_{ms} (cm)	0.10	0.10	0.10	0.10	0.10
h_{ts} (cm)	0.10	0.10	0.10	0.10	0.10
h_{bs} (cm)	0.10	0.30	0.10	0.30	0.10
h_{tc} (cm)	1.50	1.50	0.60	1.50	0.60
h_{bc} (cm)	1.50	1.50	2.40	1.50	2.40
d (cm)	2.12	2.12	2.12	2.12	2.12
r (cm)	0.20	0.20	0.20	0.20	0.20
Material	Steel–Al	Al–Al	Al–Al	Steel–Al	Steel–Al

5.1 Convergence and comparison studies

Table 2 shows the convergence of the maximum linear deflections for case I with $q_0 = +142300$ N/m^2 . With the increase of the number of polynomial terms N from 3 to 6, the maximum linear deflections are convergent and match with FEM results for each boundary conditions.

Table 3 presents the convergence of the maximum nonlinear deflections with respect to the number of polynomial terms N for case I with $q_0 = +142300$ N/m^2 . With the increase of polynomial terms N from 3 to 6, the maximum nonlinear deflections are convergent and agree well with the FEM results. Therefore, the value N is selected as 6 in the Ritz model for the following analysis.

To validate the present Ritz model, Fig. 5 compares the nonlinear load *vs.* deflection curves of the isotropic H–H beam with the results given by Mirzaei and Kiani (2015). The length to thickness ratio and Poisson's ratio of the homogeneous isotropic beam are 20 and 0.32, respectively. The thickness and the Young's modulus of the beam are 0.1 m and 210 GPa, respectively. From Fig. 5, it was observed that both

the present Ritz results and FEM results coincide well with the results given by Mirzaei and Kiani (2015).

Table 2. Convergence and comparison of maximum linear deflections (cm) of double-layer LTCSBs under three different boundary conditions for case I $\left(q_0 = +142300\ \mathrm{N/m^2}\right)$.

N	H–H	C–H	C–C
3	2.6383	1.6714	0.8408
4	3.4547	1.6717	0.8402
5	3.4637	1.6724	0.8418
6	3.4547	1.6721	0.8428
FEM	3.5350	1.6950	0.8627

Table 3. Convergence and comparison of maximum nonlinear deflections (cm) of double-layer LTCSBs under three different boundary conditions for case I $\left(q_0 = +142300\ \mathrm{N/m^2}\right)$.

N	H–H	C–H	C–C
3	2.7386	1.6143	0.8131
4	2.9145	1.6246	0.8193
5	2.9145	1.6311	0.8200
6	2.9121	1.6318	0.8223
FEM	2.9090	1.6570	0.8217

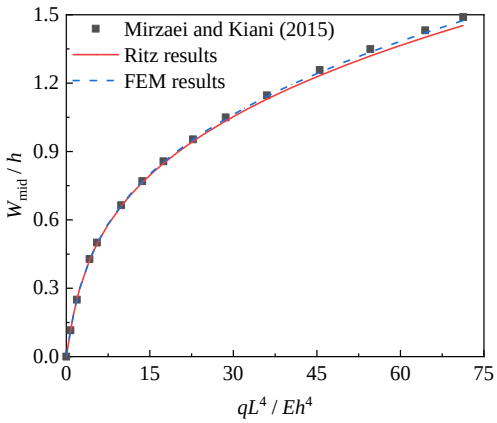

Figure 5. Nonlinear load *vs*. deflection curves for an isotropic H–H beam.

In order to validate the FEM results obtained in this study, Fig. 6 compares the maximum deflections obtained in present FEM simulation and the results given in Nampally et al. (2019) for C–C corrugated core sandwich beams. The corrugated core sandwich beam consisting of 1×30 cells, and its length is 15.9

m. The material properties of steel are $E_{\text{steel}} = 210$ GPa, $\nu_{\text{steel}} = 0.3$. The uniform load is applied with a step increment of $\Delta q_0 = 50$ N/m until a maximum load reaches 1000 N. It is observed that the present FEM results agree well with Nampally et al.'s (2019) results.

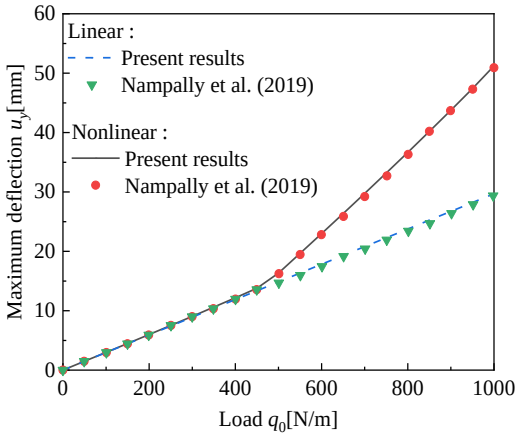

Figure 6. Linear and nonlinear maximum deflections of C–C corrugated core sandwich beam.

5.2 Effect of the loading direction

Fig. 7 shows both theorical results and FEM results on the positive maximum nonlinear deflections of unsymmetric double-layer LTCSBs for cases I, II, and III. The differences between the two methods are minor for most points, which validates the present theoretical model. However, as shown in Fig. 7(a), the relative errors for C–C and C–H beams become significant under high load due to the occurrence of local buckling. In this case, the results obtained by FEM are larger than those obtained by the theoretical model. To display the local buckling intuitively, Fig. 8 displays the FEM results for case I under the C–C boundary condition with $q_0^* = +0.001$. The local buckling occurs near the clamped ends of top face sheet for C–C double-layer LTCSBs. A similar phenomenon was also observed by Nampally et al. (2019). Note that FEM can capture the local buckling phenomenon, which cannot be predicted by the theoretical model. Therefore, in the following discussion, the results that exhibit local buckling are obtained using FEM, while other results are determined using the theoretical model.

Fig. 9 presents the negative and positive nonlinear load *vs.* deflection curves for cases I, II, and III double-layer LTCSBs under H–H, C–H, and C–C boundary conditions. For H–H and C–H beams, it was found that the magnitudes of maximum nonlinear deflections are different corresponding to the applied loads $+q_0^*$ and $-q_0^*$ in all three cases. However, for C–C double-layer LTCSBs, the loading direction has

no influence on the magnitude of maximum nonlinear deflection. This is due to the bending-extension coupling of double-layer LTCSBs under H–H or C–H boundary conditions (Singh, Rao and Iyengar 1995), whereas there is no bending-extension coupling in double-layer LTCSBs under C–C boundary condition. In present analysis, the bending-extension coupling originated from two factors: (1) the unsymmetric material properties and structural geometry and (2) the reference plane is placed at the midplane of the mid-sheet, which is not coincided with the neutral plane of the double-layer LTCSBs.

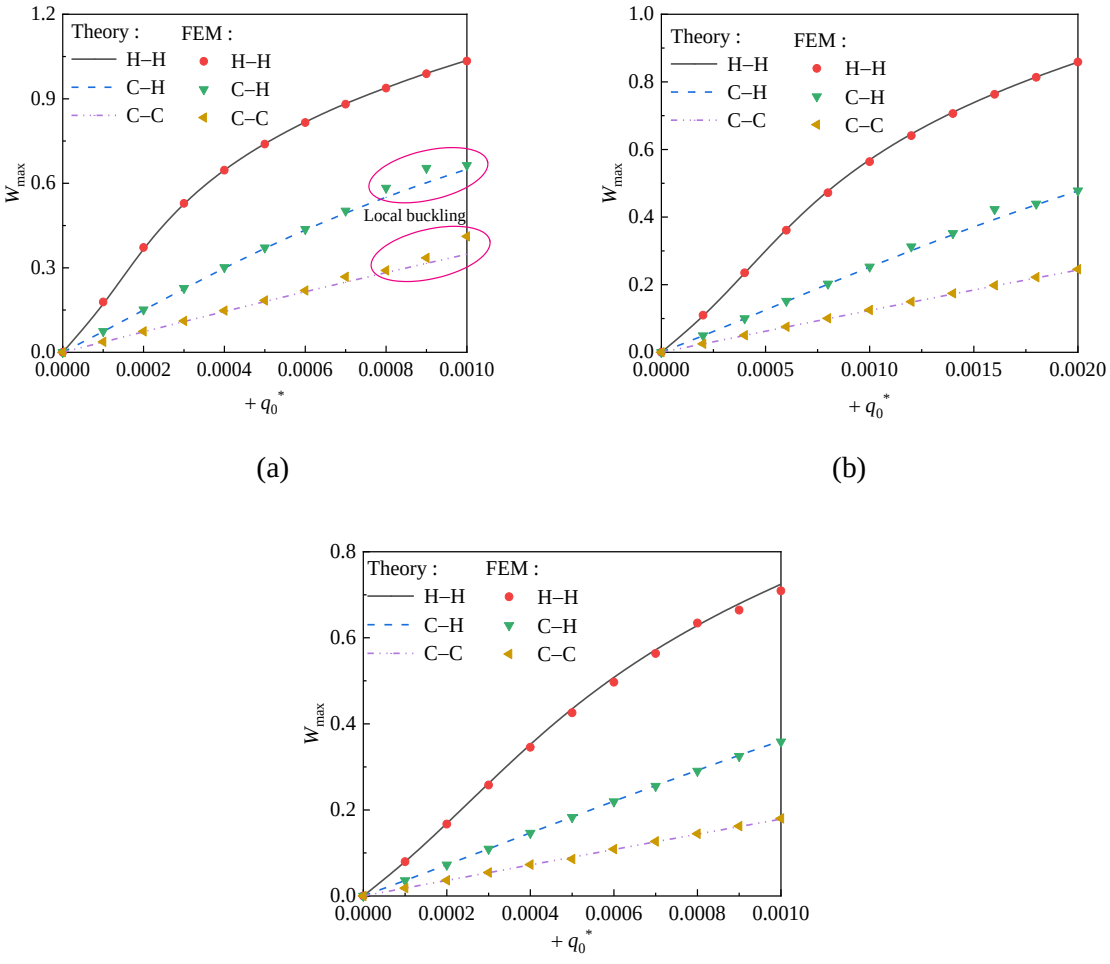

Figure 7. Positive maximum nonlinear deflections for unsymmetric double-layer LTCSBs under $+q_0^*$: (a) case I, (b) case II, and (c) case III.

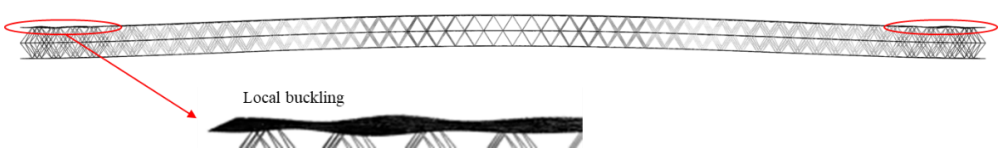

Figure 8. Local buckling of top face for case I under the C–C boundary condition with $q_0^* = +0.001$.

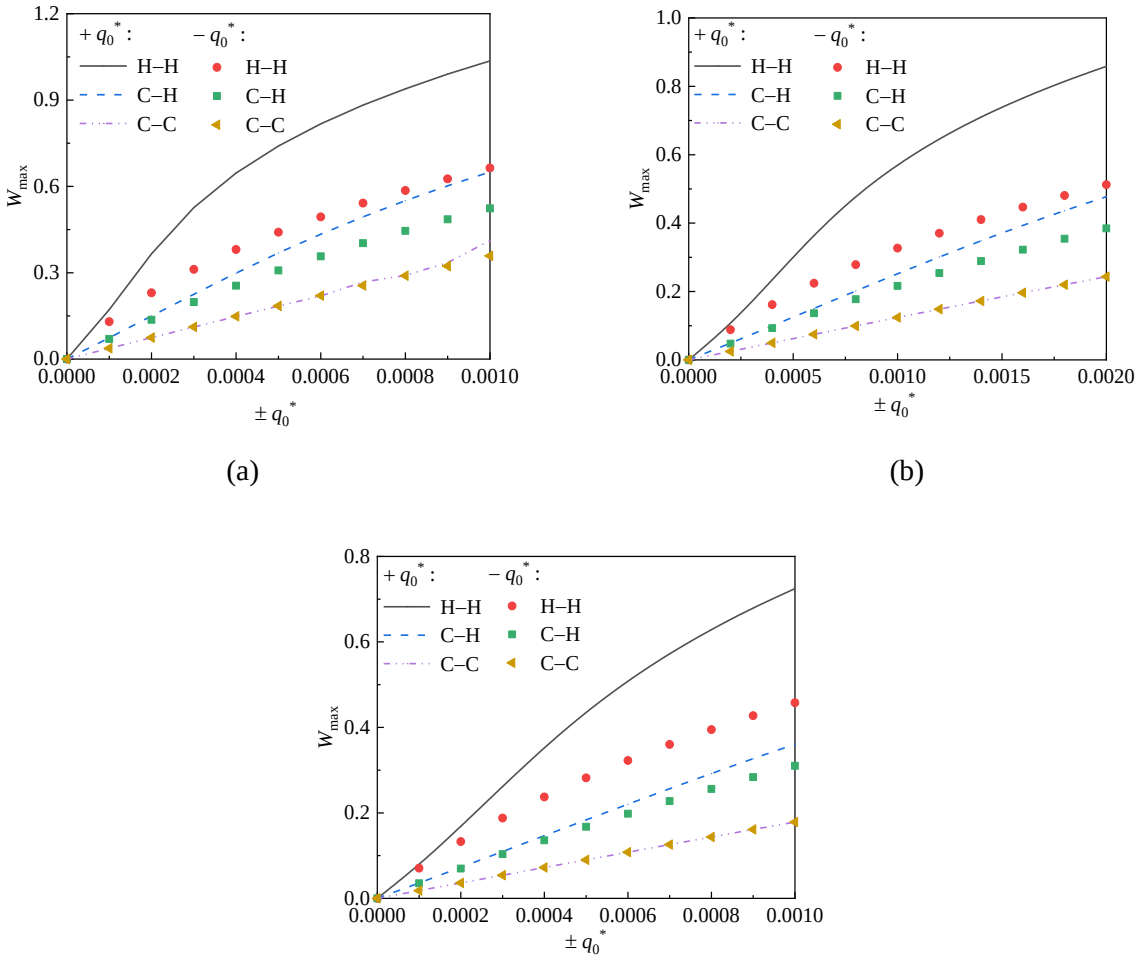

Figure 9. Positive and negative nonlinear load *vs*. deflection curves of unsymmetric double-layer LTCSBs: (a) case I, (b) case II, and (c) case III.

Furthermore, Fig. 10 shows the positive and negative nonlinear deflection curves of the beam for the cases I, II, and III subjected to the applied loads $q_0^* = \pm 0.0006$. For C–C double-layer LTCSBs, the positive and negative nonlinear deflection curves are the same, whereas the positive and negative deflection curves are different for H–H and C–H beams. These results imply that the nonlinear deflections are loading-direction dependent for unsymmetric double-layer LTCSBs with H–H or C–H boundary conditions.

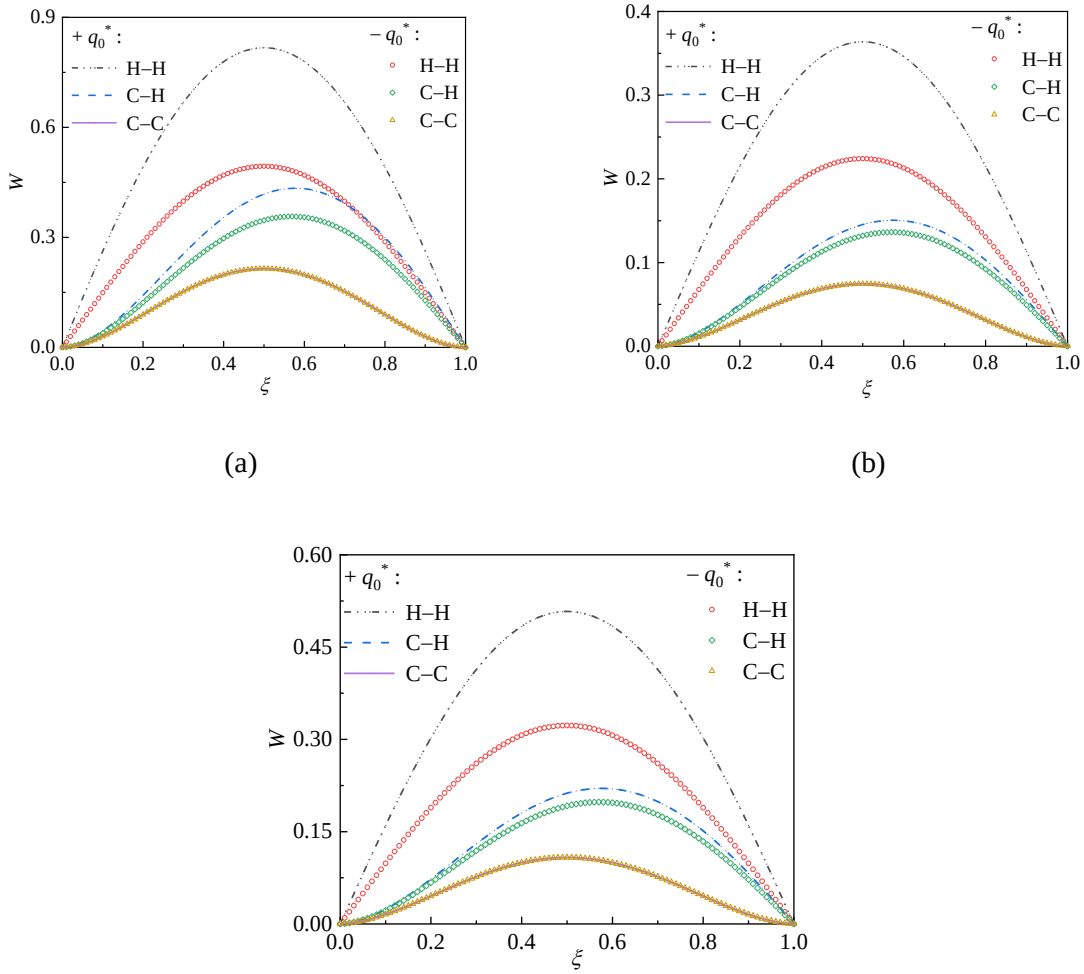

Figure 10. Positive and negative nonlinear deflection curves of unsymmetric double-layer LTCSBs with $q_0^* = \pm 0.0006$: (a) case I, (b) case II, and (c) case III.

5.3 Softening-spring nonlinearity

Fig. 11 shows the linear and nonlinear load *vs.* deflection curves of double-layer LTCSBs with the H–H boundary condition for cases I, II, and III. It is noteworthy that, for these three cases, the positive nonlinear deflection may be larger than the linear deflection at low loads, which is referring to the softening-spring nonlinearity. This phenomenon arises due to the strong bending-extension coupling effect. As the load increases, the positive nonlinear deflection becomes smaller than the linear deflection, resulting in a hardening-spring type of nonlinearity. A similar softening-spring nonlinearity phenomenon was also observed in the nonlinear bending of composite plates (Singh, Rao and Iyengar 1991) and functionally graded beams (Tam et al. 2020). Nevertheless, the negative nonlinear deflections are

consistently lower than the corresponding linear deflection.

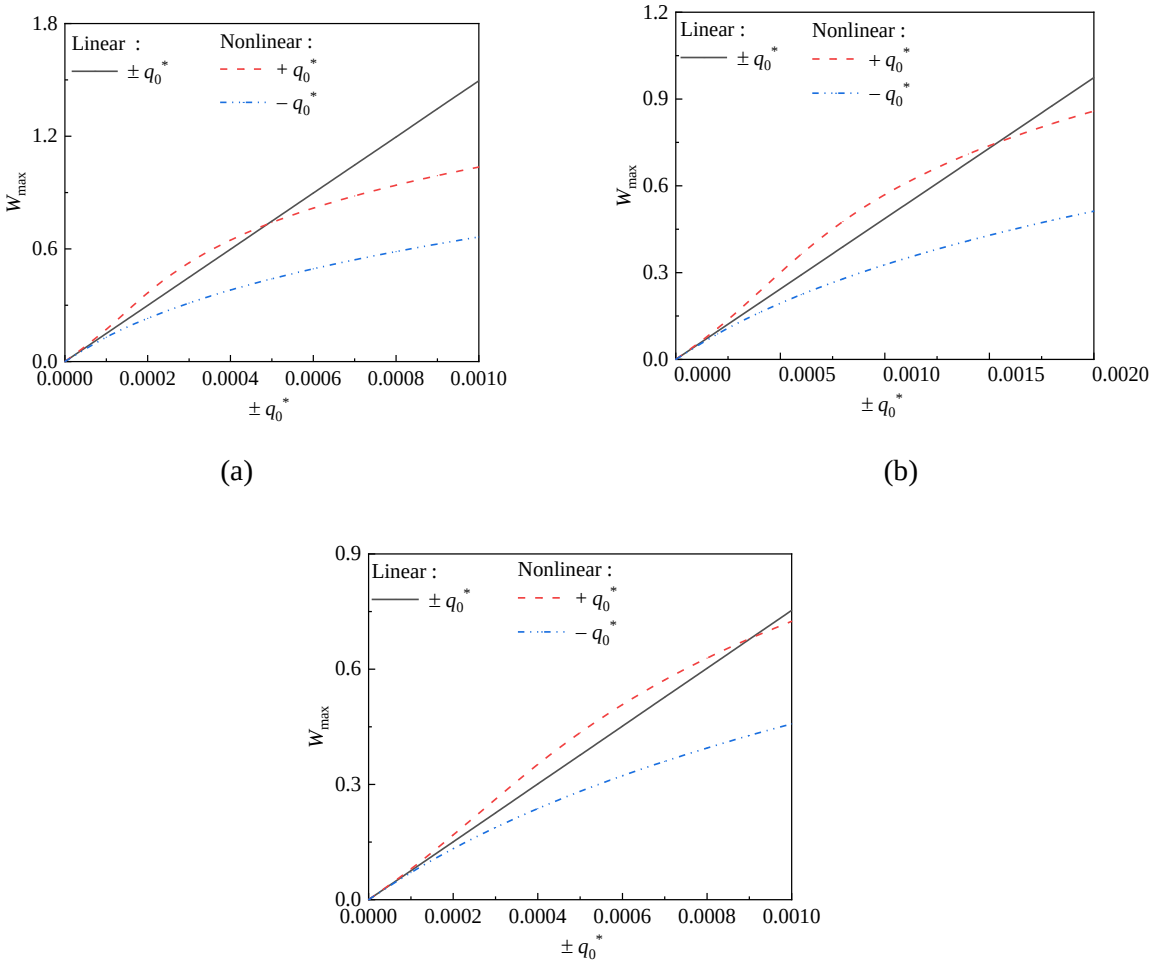

Figure 11. Linear and nonlinear load *vs*. deflection curves of H–H double-layer LTCSBs: (a) case I, (b) case II, and (c) case III.

Figs. 12 and 13 present the linear and nonlinear load *vs.* deflection curves of cases I, II, and III double-layer LTCSBs under C–H and C–C boundary conditions. For C–H double-layer LTCSBs, it was found that the positive nonlinear load-deflection curves have very slight softening-spring nonlinearity. However, for C–C double-layer LTCSBs, both positive and negative nonlinear load-deflection curves exhibiting hardening-spring nonlinearity. That is due to the clamped boundary condition, which can counterbalance the bending-extension coupling effect. Note, the slop change in the positive nonlinear load *vs.* deflection curve in Fig. 13(a) is caused by local buckling.

To explain the physical mechanism of the softening-spring nonlinearity in the nonlinear bending, Fig. 14 plots the nonlinear axial forces N_x^* of H–H double-layer LTCSBs for case II under the positive load.

For a smaller positive load ($+q_0^* = 0.0001$ and $+q_0^* = 0.0005$), it is clearly observed that the in-plane force N_x^* is compressive ($N_x^* < 0$) near the two ends of unsymmetric double-layer LTCSBs. The in-plane compressive force resulting from the bending–extension coupling effect can reduce the stiffness of structures, and then increases the deflection of unsymmetric double-layer LTCSBs (Fallah and Nosier 2008; Karimi and Fallah 2021). However, when the load is increased to $+q_0^* = 0.0009$, the in-plane force becomes tensile ($N_x^* > 0$) at the whole beam. The in-plane tensile force caused by the large deflection provides additional bending rigidity to reduce transverse deflection. That is the reason why the nonlinear deflection smaller than the linear deflection under a large load (Nosier and Fallah 2009; Sun and Chin 1988).

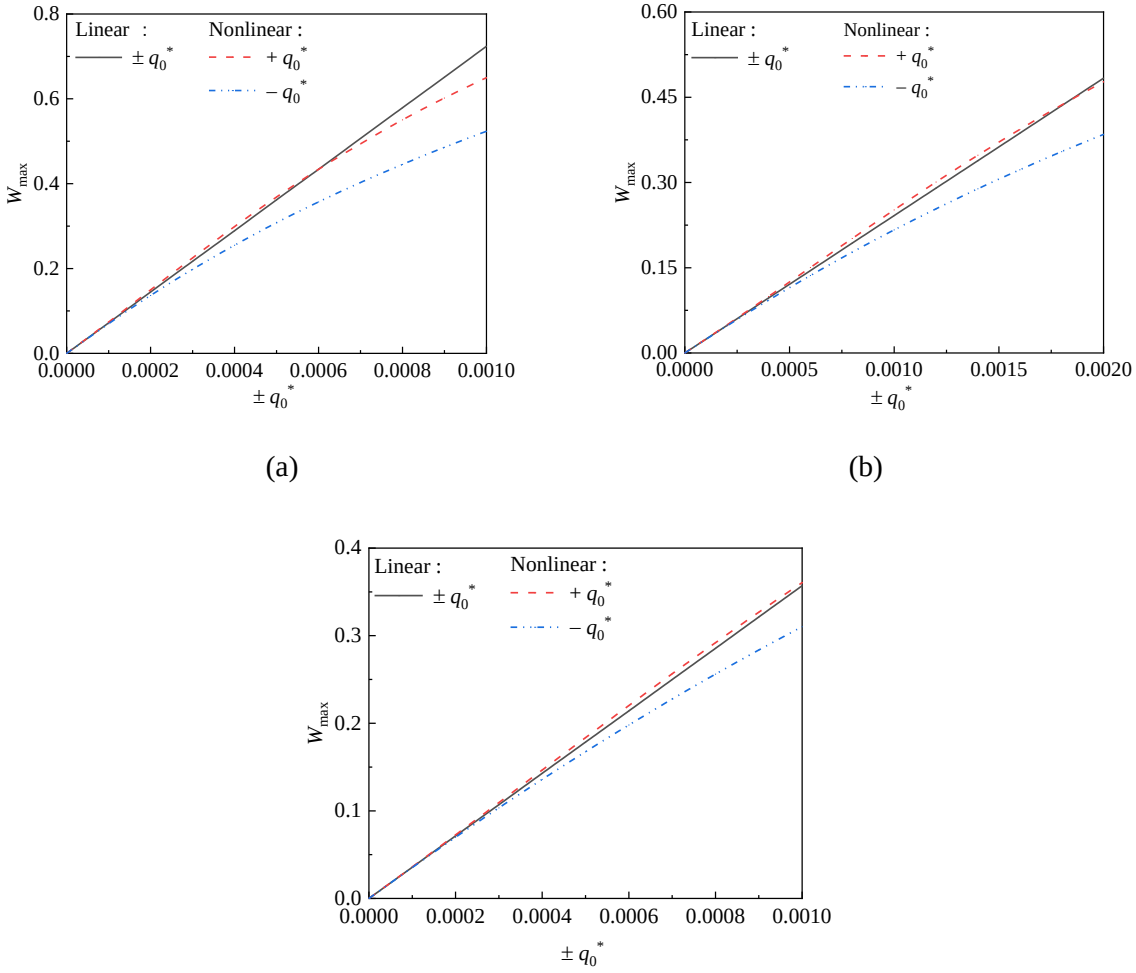

(a) (b)

(c)

Figure 12. Linear and nonlinear load *vs*. deflection curves of C–H double-layer LTCSBs: (a) case I, (b) case II, and (c) case III.

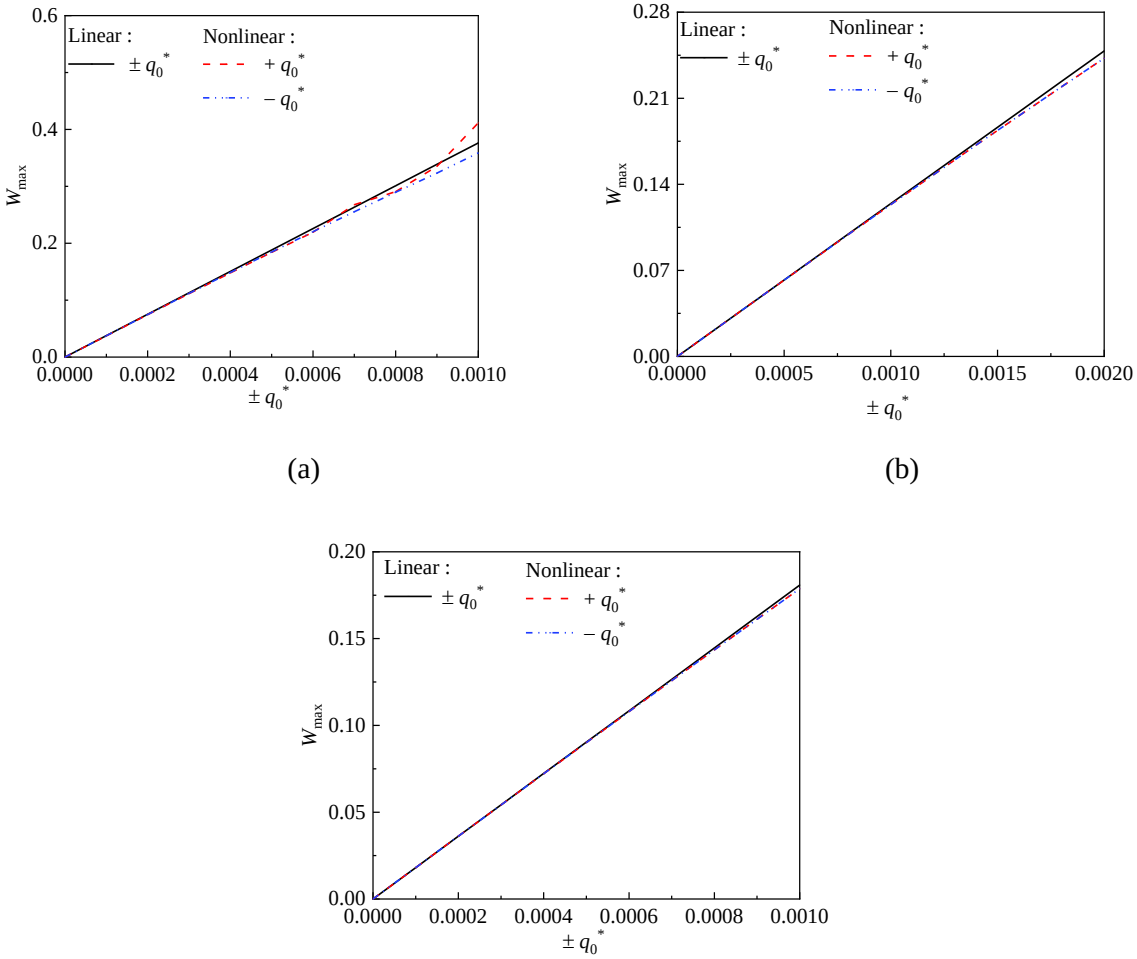

Figure 13. Linear and nonlinear load *vs.* deflection curves of C–C double-layer LTCSBs: (a) case I, (b) case II, and (c) case III.

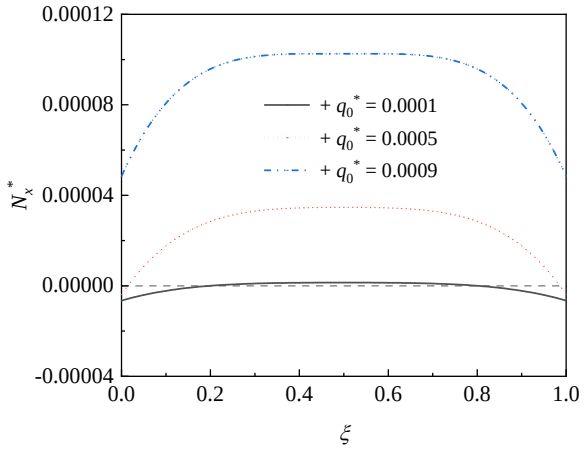

Figure 14. The nonlinear axial forces N_x^* of H–H double-layer LTCSBs for case II under the positive load.

5.4 The combined effect of material and geometry

The above analysis revealed that the positive and negative nonlinear deflections differ from beams with H–H or C–H boundary conditions due to the bending-extension coupling effect. Moreover, a slight softening-spring nonlinearity was observed for the C–H LTCSBs, while it is more prominent for the H–H LTCSBs. This subsection considers the combined effect of material properties and structural geometry, i.e., cases IV and V, which exhibit a stronger bending-extension coupling effect than cases I, II, and III. Only the H–H and C–H boundary conditions are discussed since the special softening-spring nonlinearity does not occur under C–C boundary conditions.

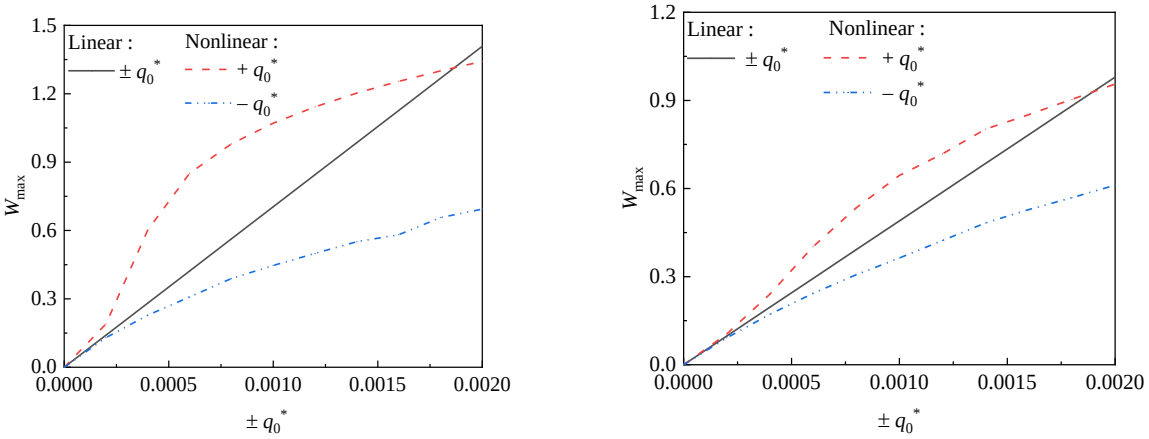

Figure 15. Linear and nonlinear load *vs*. deflection curves for case IV: (a) H–H and (b) C–H.

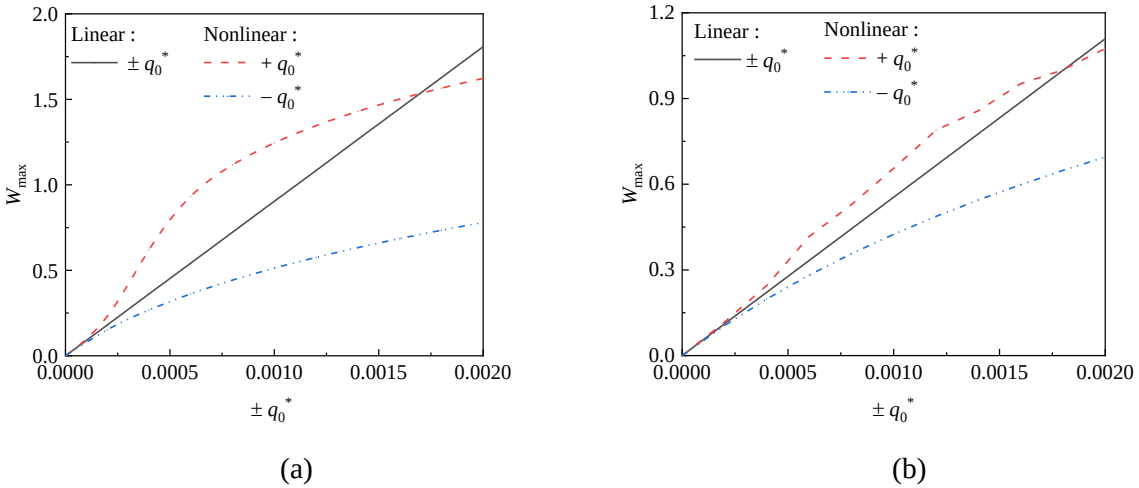

Figure 16. Linear and nonlinear load *vs*. deflection curves for case V: (a) H–H and (b) C–H.

Figs. 15 and 16 display the linear and nonlinear load *vs*. deflection curves for cases IV and V, respectively. The combined effect of material properties and structural geometry leads to a greater difference between positive and negative deflections for both H–H and C–H beams than that in cases I, II,

and III. Furthermore, the softening-spring nonlinearity for cases IV and V is more pronounced than that in cases I, II, and III. This is because the combined effect of material properties and structural geometry further strengthens the bending-extension effect in the unsymmetric LTCSBs.

6. Conclusions

This paper presents a study of the nonlinear bending behavior of unsymmetric double-layer LTCSBs. The theoretical model is established based on Allen's model and von Kármán nonlinearity. The nonlinear bending deflections of double-layer LTCSBs with different boundary conditions are obtained using the Ritz method and FEM. The effects of different load directions on the nonlinear bending behavior of the unsymmetric double-layer LTCSB are discussed in details in this paper. The findings of this study reveal that:

(1) The positive and negative nonlinear deflections of unsymmetric LTCSBs with H–H and C–H boundary conditions exhibit different behaviour for all cases. Moreover, the difference between these two deflections increases significantly in cases IV and V.

(2) Both the H–H and C–H unsymmetric double-layer LTCSBs may exhibit softening-spring nonlinearity at low loads, following by a transition to hardening. Moreover, the softening-spring nonlinearity in cases IV and V is more pronounced than that in cases I–III.

(3) The positive and negative nonlinear deflections of C–C unsymmetric double-layer LTCSBs remain constant for the same magnitude load, exhibiting only hardening-spring nonlinearity in each case.

(4) The nonlinear deflections of C–C unsymmetric double-layer LTCSBs may be larger than the linear deflections at large load due to the occurrence of local buckling in top face sheets, which cannot be captured by the theorical model.

Acknowledgments

This work is funded by the National Natural Science Foundation of China (Nos. 11725207 and 12021002).

Appendix A

Rewrite the form of trial functions including the boundary condition as

$U(\xi)=\sum_{j=1}^{N}A_j\Xi_{1j}$, $W(\xi)=\sum_{j=1}^{N}B_j\Xi_{1j}$, $\varphi(\xi)=\sum_{j=1}^{N}C_j\Xi_{2j}$.

The elements of transvers uniform load is

$\boldsymbol{q}_{0(1,j)}=q_0^*\int_0^1\Xi_{1j}\mathrm{d}\xi$, where $j=1,2,...,N$.

The elements of linear stiffness matrix $[\mathbf{K_L}]_{3N\times 3N}$ are

$$[\mathbf{K_L}]_{(k,j)}=\int_0^1 k_1\frac{\mathrm{d}\Xi_{1j}}{\mathrm{d}\xi}\frac{\mathrm{d}\Xi_{1k}}{\mathrm{d}\xi}\mathrm{d}\xi\ ,\ [\mathbf{K_L}]_{(k,j+N)}=\frac{1}{2}\int_0^1 k_7\frac{\mathrm{d}^2\Xi_{1j}}{\mathrm{d}\xi^2}\frac{\mathrm{d}\Xi_{1k}}{\mathrm{d}\xi}\mathrm{d}\xi\ ,$$

$$[\mathbf{K_L}]_{(k,j+2N)}=\frac{1}{2}\int_0^1 k_3\frac{\mathrm{d}\Xi_{2j}}{\mathrm{d}\xi}\frac{\mathrm{d}\Xi_{1k}}{\mathrm{d}\xi}\mathrm{d}\xi\ ,\ [\mathbf{K_L}]_{(k+N,j)}=\frac{1}{2}\int_0^1 k_7\frac{\mathrm{d}^2\Xi_{1k}}{\mathrm{d}\xi^2}\frac{\mathrm{d}\Xi_{1j}}{\mathrm{d}\xi}\mathrm{d}\xi\ ,$$

$$[\mathbf{K_L}]_{(k+N,j+N)}=\int_0^1\left(k_4\frac{\mathrm{d}^2\Xi_{1k}}{\mathrm{d}\xi^2}\frac{\mathrm{d}^2\Xi_{1j}}{\mathrm{d}\xi^2}+k_5\frac{\mathrm{d}\Xi_{1k}}{\mathrm{d}\xi}\frac{\mathrm{d}\Xi_{1j}}{\mathrm{d}\xi}\right)\mathrm{d}\xi\ ,$$

$$[\mathbf{K_L}]_{(k+N,j+2N)}=\frac{1}{2}\int_0^1\left(k_6\frac{\mathrm{d}^2\Xi_{1k}}{\mathrm{d}\xi^2}\frac{\mathrm{d}\Xi_{2j}}{\mathrm{d}\xi}-k_{12}\Xi_{2j}\frac{\mathrm{d}\Xi_{1k}}{\mathrm{d}\xi}\right)\mathrm{d}\xi\ ,$$

$$[\mathbf{K_L}]_{(k+2N,j)}=\frac{1}{2}\int_0^1 k_3\frac{\mathrm{d}\Xi_{1j}}{\mathrm{d}\xi}\frac{\mathrm{d}\Xi_{2k}}{\mathrm{d}\xi}\mathrm{d}\xi\ ,\ [\mathbf{K_L}]_{(k+2N,j+N)}=\frac{1}{2}\int_0^1\left(k_6\frac{\mathrm{d}^2\Xi_{1j}}{\mathrm{d}\xi^2}\frac{\mathrm{d}\Xi_{2k}}{\mathrm{d}\xi}-k_{12}\Xi_{2k}\frac{\mathrm{d}\Xi_{1j}}{\mathrm{d}\xi}\right)\mathrm{d}\xi\ ,$$

$$[\mathbf{K_L}]_{(k+2N,j+2N)}=\int_0^1\left(k_2\frac{\mathrm{d}\Xi_{2k}}{\mathrm{d}\xi}\frac{\mathrm{d}\Xi_{2j}}{\mathrm{d}\xi}+k_{13}\Xi_{2k}\Xi_{2j}\right)\mathrm{d}\xi\ .$$

The elements of the matrix $[\mathbf{K_{NL1}}]_{3N\times 3N}$ are

$$[\mathbf{K_{NL1}}]_{(k,j+N)}=\frac{1}{2}\int_0^1 k_9\frac{\mathrm{d}W}{\mathrm{d}\xi}\frac{\mathrm{d}\Xi_{1j}}{\mathrm{d}\xi}\frac{\mathrm{d}\Xi_{1k}}{\mathrm{d}\xi}\mathrm{d}\xi\ ,\ [\mathbf{K_{NL1}}]_{(k+N,j)}=\int_0^1 k_9\frac{\mathrm{d}W}{\mathrm{d}\xi}\frac{\mathrm{d}\Xi_{1j}}{\mathrm{d}\xi}\frac{\mathrm{d}\Xi_{1k}}{\mathrm{d}\xi}\mathrm{d}\xi\ ,$$

$$[\mathbf{K_{NL1}}]_{(k+N,j+N)}=\frac{1}{2}\int_0^1 k_{11}\left(\frac{\mathrm{d}W}{\mathrm{d}\xi}\frac{\mathrm{d}\Xi_{1j}}{\mathrm{d}\xi}\frac{\mathrm{d}^2\Xi_{1k}}{\mathrm{d}\xi^2}+\frac{\mathrm{d}^2W}{\mathrm{d}\xi^2}\frac{\mathrm{d}\Xi_{1j}}{\mathrm{d}\xi}\frac{\mathrm{d}\Xi_{1k}}{\mathrm{d}\xi}+\frac{\mathrm{d}W}{\mathrm{d}\xi}\frac{\mathrm{d}\Xi_{1k}}{\mathrm{d}\xi}\frac{\mathrm{d}^2\Xi_{1j}}{\mathrm{d}\xi^2}\right)\mathrm{d}\xi\ ,$$

$$[\mathbf{K_{NL1}}]_{(k+N,j+2N)}=\int_0^1 k_{10}\frac{\mathrm{d}W}{\mathrm{d}\xi}\frac{\mathrm{d}\Xi_{2j}}{\mathrm{d}\xi}\frac{\mathrm{d}\Xi_{1k}}{\mathrm{d}\xi}\mathrm{d}\xi\ ,\ [\mathbf{K_{NL1}}]_{(k+2N,j+N)}=\frac{1}{2}\int_0^1 k_{10}\frac{\mathrm{d}W}{\mathrm{d}\xi}\frac{\mathrm{d}\Xi_{1j}}{\mathrm{d}\xi}\frac{\mathrm{d}\Xi_{2k}}{\mathrm{d}\xi}\mathrm{d}\xi\ .$$

The element of the matrix $[\mathbf{K_{NL2}}]_{3N\times 3N}$ is

$$[\mathbf{K_{NL2}}]_{(k+N,j+N)}=\int_0^1 k_8\left(\frac{\mathrm{d}W}{\mathrm{d}\xi}\right)^2\frac{\mathrm{d}\Xi_{1j}}{\mathrm{d}\xi}\frac{\mathrm{d}\Xi_{1k}}{\mathrm{d}\xi}\mathrm{d}\xi\ ,$$

in which $j,k=1,2,...,N$.

The coefficients in stiffness matrixes are

$k_1 = \bar{A}_{11},\ k_2 = \bar{A}_{13},\ k_3 = -2\bar{A}_{12}, k_4 = \zeta_2{}^2\left(\bar{A}_{13} - 2\bar{B}_{12} + \bar{D}_{11}\right),\ k_5 = \bar{A}_{00},$

$k_6 = 2\zeta_2\left(\bar{B}_{12} - \bar{A}_{13}\right),\ k_7 = -2\zeta_2\left(\bar{B}_{11} - \bar{A}_{12}\right),\ k_8 = \frac{\zeta_2{}^2}{2}\bar{A}_{11},\ k_9 = \zeta_2\bar{A}_{11},$

$k_{10} = -\zeta_2\bar{A}_{12},\ k_{11} = -\zeta_2{}^2\left(\bar{B}_{11} - \bar{A}_{12}\right),\ k_{12} = \frac{2}{\zeta_2}\bar{A}_{00},\ k_{13} = \frac{1}{\zeta_2{}^2}\bar{A}_{00},$

where the dimensionless corresponding coefficients are

$\bar{A}_{00} = \bar{S}_{tc} + \bar{S}_{bc},\ \bar{A}_{11} = \bar{A}_{ts} + \bar{A}_{ms} + \bar{A}_{bs},\ \bar{A}_{12} = \zeta_3\bar{A}_{ts} - \zeta_1\bar{A}_{bs},$

$\bar{A}_{13} = \zeta_3{}^2\bar{A}_{ts} + \zeta_1{}^2\bar{A}_{bs},\ \bar{B}_{11} = \bar{B}_{ts} + \bar{B}_{ms} + \bar{B}_{bs},\ \bar{B}_{12} = \zeta_3\bar{B}_{ts} - \zeta_1\bar{B}_{bs},$

$\bar{D}_{11} = \bar{D}_{ts} + \bar{D}_{ms} + \bar{D}_{bs}.$

References

Li, J. G., X. L. An, J. J. Liang, Y. Z. Zhou, and X. F. Sun. 2022. Recent advances in the stereolithographic three-dimensional printing of ceramic cores: Challenges and prospects. *Journal of Materials Science & Technology* 117: 79–98. doi: 10.1016/j.jmst.2021.10.041.

Yang, W., J. Xiong, L. J. Feng, C. Pei, and L. Z. Wu. 2020. Fabrication and mechanical properties of three-dimensional enhanced lattice truss sandwich structures. *Journal of Sandwich Structures & Materials* 22 (5): 1594–1611. doi: 10.1177/1099636218789602.

Lou, J., B. Wang, L. Ma, and L. Z. Wu. 2013. Free vibration analysis of lattice sandwich beams under several typical boundary conditions. *Acta Mechanica Solida Sinica* 26 (5): 458–467. doi: 10.1016/S0894-9166(13)60041-5.

Xu, M. H., and Z. P. Qiu. 2013. Free vibration analysis and optimization of composite lattice truss core sandwich beams with interval parameters. *Composite Structures* 106: 85–95. doi: 10.1016/j.compstruct.2013.05.048.

Zhao, Z., S. R. Wen, and F. M. Li. 2018. Vibration analysis of multi-span lattice sandwich beams using the assumed mode method. *Composite Structures* 185: 716–727. doi: 10.1016/j.compstruct.2017.11.069.

Guo, Z. K., G. B. Hu, V. Sorokin, Y. Yang, and L. H. Tang. 2021. Sound transmission through sandwich plate with hourglass lattice truss core. *Journal of Sandwich Structures & Materials* 23 (6): 1902–1928. doi: 10.1177/1099636220906819.

Nasrullah, A. I. H., S. P. Santosa, and T. Dirgantara. 2020. Design and optimization of crashworthy components based on lattice structure configuration. *Structures* 26: 969–981. doi:

10.1016/j.istruc.2020.05.001.

Wadley, H. N. G., K. P. Dharmasena, Y. C. Chen, P. Dudt, D. Knight, R. Charette, and K. Kiddy. 2008. Compressive response of multilayered pyramidal lattices during underwater shock loading. *International Journal of Impact Engineering* 35 (9): 1102–1114. doi: 10.1016/j.ijimpeng.2007.06.009.

Evans, A. G., J. W. Hutchinson, N. A. Fleck, M. F. Ashby, and H. N. G. Wadley. 2001. The topological design of multifunctional cellular metals. *Progress in Materials Science* 46 (3–4): 309–327. doi: 10.1016/S0079-6425(00)00016-5.

Vinson, J. R. 2005. *Sandwich Structures: Past, Present, and Future*. Dordrecht, The Netherlands: Springer. doi: 10.1007/1-4020-3848-8_1.

Zhang, L., S. Feih, S. Daynes, Y. Q. Wang, M. Y. Wang, J. Wei, and W. F. Lu. 2018. Buckling optimization of Kagome lattice cores with free-form trusses. *Materials & Design* 145: 144–155. doi: 10.1016/j.matdes.2018.02.026.

Xu, G. D., F. Yang, T. Zeng, S. Cheng, and Z. H. Wang. 2016. Bending behavior of graded corrugated truss core composite sandwich beams. *Composite Structures* 138: 342–351. doi: 10.1016/j.compstruct.2015.11.057.

Yin, S., L. Z. Wu, L. Ma, and S. Nutt. 2011. Pyramidal lattice sandwich structures with hollow composite trusses. *Composite Structures* 93 (12): 3104–3111. doi: 10.1016/j.compstruct.2011.06.025.

Li, M., S. J. Du, F. M. Li, and X. J. Jing. 2020. Vibration characteristics of novel multilayer sandwich beams: Modelling, analysis and experimental validations. *Mechanical Systems and Signal Processing* 142: 106799. doi: 10.1016/j.ymssp.2020.106799.

Yang, L. H., L. Sui, Y. L. Dong, X. Y. Li, F. Zi, Z. X. Zhang, S. J. Yang, J. S. Yang, and L. Z. Wu. 2021. Quasi-static and dynamic behavior of sandwich panels with multilayer gradient lattice cores. *Composite Structures* 255: 112970. doi: 10.1016/j.compstruct.2020.112970.

Ni, C. Y., R. Hou, B. Han, F. Jin, G. W. Ma, and T. J. Lu. 2017. Normal and oblique projectile impact of double-layered pyramidal lattice truss structures filled with ceramic insertions. *Journal of Thermoplastic Composite Materials* 30 (8): 1136–1156. doi: 10.1177/0892705715618739.

Wang, D., X. J. Zhang, Z. C. Dong, G. W. Li, and H. Y. Huang. 2022. Thermo-mechanical performance of 3D-printed TC4 hierarchical lattice-truss-core sandwich structures in high temperature conditions. *Mechanics of Advanced Materials and Structures*. doi: 10.1080/15376494.2022.2073407.

Xiong, J., R. Ghosh, L. Ma, H. Ebrahimi, A. M. S. Hamouda, A. Vaziri, and L. Wu. 2014. Bending

behavior of lightweight sandwich-walled shells with pyramidal truss cores. *Composite Structures* 116: 793–804. doi: 10.1016/j.compstruct.2014.06.006.

Yuan, W., H. W. Song, L. L. Lu, and C. G. Huang. 2016. Effect of local damages on the buckling behaviour of pyramidal truss core sandwich panels, *Composite Structures* 149: 271–278. doi: 10.1016/j.compstruct.2016.04.031.

Fan, H. L., F. H. Meng, and W. Yang. 2006. Mechanical behaviors and bending effects of carbon fiber reinforced lattice materials. *Archive of Applied Mechanics* 75 (10–12): 635–647. doi: 10.1007/s00419-006-0032-x.

Lou, J., L. Ma, and L. Z. Wu. 2012. Free vibration analysis of simply supported sandwich beams with lattice truss core. *Materials Science and Engineering B-Advanced Functional Solid-State Materials* 177 (19): 1712–1716. doi: 10.1016/j.mseb.2012.02.003.

Li, C, C. X. Zhu, C. W. Lim, and S. Li. 2022. Nonlinear in-plane thermal buckling of rotationally restrained functionally graded carbon nanotube reinforced composite shallow arches under uniform radial loading. *Applied Mathematics and Mechanics-English Edition* 43 (12): 1821–1840. doi: 10.1007/s10483-022-2917-7.

Chai, Y. Y., S. J. Du, F. M. Li, and C. Z. Zhang. 2021. Vibration characteristics of simply supported pyramidal lattice sandwich plates on elastic foundation: Theory and experiments. *Thin-Walled Structures* 166: 108116. doi: 10.1016/j.tws.2021.108116.

Zhang, L., Y. F. Chen, R. J. He, X. J. Bai, K. Q. Zhang, S. G. Ai, Y. Z. Yang, and D. N. Fang. 2020. Bending behavior of lightweight C/SiC pyramidal lattice core sandwich panels. *International Journal of Mechanical Sciences* 171: 105409. doi: 10.1016/j.ijmecsci.2019.105409.

Xiong, J., L. Ma, L. Z. Wu, J. Y. Liu, and A. Vaziri. 2011. Mechanical behavior and failure of composite pyramidal truss core sandwich columns. *Composites Part B-Engineering* 42 (4): 938–945. doi: 10.1016/j.compositesb.2010.12.021.

Chen, J. W., Y. Q. Liu, W. Liu, and X. Y. Su. 2013. Thermal buckling analysis of truss-core sandwich plates. *Applied Mathematics and Mechanics* 34 (10): 1177–1186. doi: 10.1007/s10483-013-1737-9.

Li, D. H., R. P. Wang, R. L. Qian, Y. Liu, and G. H. Qing. 2016. Static response and free vibration analysis of the composite sandwich structures with multi-layer cores. *International Journal of Mechanical Sciences* 111: 101–115. doi: 10.1016/j.ijmecsci.2016.04.002.

Cao, B. T., B. Hou, Y. L. Li, and H. Zhao. 2017. An experimental study on the impact behavior of

multilayer sandwich with corrugated cores. *International Journal of Solids and Structures* 109: 33–45. doi: 10.1016/j.ijsolstr.2017.01.005.

Nampally, P., A. T. Karttunen, and J. N. Reddy. 2019. Nonlinear finite element analysis of lattice core sandwich beams. *European Journal of Mechanics A-Solids* 74: 431–439. doi: 10.48550/arXiv.1901.00775.

Zhang, W., C. X. Wang, Y. W. Wang, J. J. Mao, and Y. Z. Liu. 2022. Nonlinear vibration responses of lattice sandwich beams with FGM facesheets based on an improved thermo-mechanical equivalent model. *Structures* 44: 920–932. doi.: 10.1016/j.istruc.2022.08.052.

Chai, Y. Y., F. M. Li, and Z. G. Song. 2019. Nonlinear flutter suppression and thermal buckling elimination for composite lattice sandwich panels. *AIAA Journal* 57 (11): 4863–4872, doi.: 10.2514/1.J058307.

Chai, Y. Y., F. M. Li, and Z. G. Song. 2019. Nonlinear vibrations, bifurcations and chaos of lattice sandwich composite panels on Winkler–Pasternak elastic foundations with thermal effects in supersonic airflow. *Meccanica* 54 (7): 919–944. doi: 10.1007/s11012-019-00995-4.

Li, C., H. S. Shen, and H. Wang. 2020. Full-scale finite element modeling and nonlinear bending analysis of sandwich plates with functionally graded auxetic 3D lattice core. *Journal of Sandwich Structures & Materials* 23 (7): 3113–3138. doi: 10.1177/1099636220924657.

Li, C., H. S. Shen, and H. Wang. 2020. Large amplitude vibration of sandwich plates with functionally graded auxetic 3D lattice core. *International Journal of Mechanical Science* 174: 105472. doi: 10.1016/j.ijmecsci.2020.105472.

Hao, N., L. F. Zhu, Z. M. Wu, and L. L. Ke. 2023. Softening-spring nonlinearity in large amplitude vibration of unsymmetric double-layer lattice truss core sandwich beams. *Thin-Walled Structures* 182: 110164. doi: 10.1016/j.tws.2022.110164.

Liu, J. Y., L. L. Xiang, and T. Kan. 2015. The effect of temperature on the bending properties and failure mechanism of composite truss core sandwich structures. *Composites Part A-Applied Science and Manufacturing* 79: 146–154, doi: 10.1016/j.compositesa.2015.09.017.

Liu, L. X., W. Y. Yang, Y. Y. Chai, and G. F. Zhai. 2021. Vibration and thermal buckling analyses of multi-span composite lattice sandwich beams. *Archive of Applied Mechanics* 91 (6): 2601–2616. doi: 10.1007/s00419-021-01908-2.

Allen, H. G. 1969. *Analysis and Design of Structural Sandwich Panels*. Oxford: Pergamon Press. doi:

10.1016/C2013-0-02134-2.

Kitipornchai, S., L. L. Ke, J. Yang, and Y. Xiang. 2009. Nonlinear vibration of edge cracked functionally graded Timoshenko beams. *Journal of Sound and Vibration* 324 (3–5): 962–982, doi: 10.1016/j.jsv.2009.02.023.

Chen, J. E., W. Zhang, M. Sun, and M. H. Yao. 2016. Free vibration and hardening behavior of truss core sandwich beam. *Shock and Vibration* 2016: 1–13. doi: 10.1155/2016/7348518.

Ke, L. L., J. Yang, and S. Kitipornchai. 2010. Nonlinear free vibration of functionally graded carbon nanotube- reinforced composite Timoshenko beam. *Composite Structures* 92 (3): 676–683. doi: 10.1016/j.compstruct.2009.09.024.

Liew, K. M., C. M. Wang, Y. Xiang, and S. Kitipornchai. 1998. *Vibration of Mindlin plates: programming the p-version ritz method*. Oxford: Elsevier Science. doi: 10.1016/B978-0-08-043341-7.X5000-6.

Anirudh, B., T. Ben Zineb, O. Polit, M. Ganapathi, and G. Prateek. 2020. Nonlinear bending of porous curved beams reinforced by functionally graded nanocomposite graphene platelets applying an efficient shear flexible finite element approach. *International Journal of Non-Linear Mechanics* 119: 103346. doi: 10.1016/j.ijnonlinmec.2019.103346.

Radice, J. J. 2012. On the effect of local boundary condition details on the natural frequencies of simply-supported beams: Eccentric pin supports. *Mechanics Research Communications* 39 (1): 1–8. doi: 10.1016/j.mechrescom.2011.08.007.

Mirzaei, M., and Y. Kiani. 2015. Snap-through phenomenon in a thermally postbuckled temperature dependent sandwich beam with FG-CNTRC face sheets. *Composite Structures* 134: 1004–1013. doi.: 10.1016/j.compstruct.2015.09.003.

Singh, G., G. V. Rao, and N. Iyengar. 1995. Finite element analysis of the non-linear vibration of moderately thick unsymmetrically laminated composite plates. *Journal of Sound and Vibration* 181 (2): 315–329. doi: 10.1006/jsvi.1995.0142.

Singh, G., G. V. Rao, and N. G. R. Iyengar. 1991. Some observations on the large deflection bending of rectangular antisymmetric cross-ply plates. *Composite Structures* 18 (1): 77–91. doi: 10.1016/0263-8223(91)90015-Q.

Tam, M. F., Z. C. Yang, S. Y. Zhao, H. N. Zhang, Y. Y. Zhang, and J. Yang. 2020. Nonlinear bending of elastically restrained functionally graded graphene nanoplatelet reinforced beams with an open edge crack. *Thin-Walled Structures* 156: 106972. doi: 10.1016/j.tws.2020.106972.

Fallah, F., and A. Nosier. 2008. Non-linear thermo-mechanical cylindrical bending of functionally graded plates. *Proceedings of the Institution of Mechanical Engineers, Part C* 222 (3): 305–318. doi: 10.1243/09544062JMES772.

Karimi, M. H., and F. Famida. 2021. Analytical non-linear analysis of functionally graded sandwich solid/annular sector plates. *Composite Structures* 275: 114420. doi: 10.1016/j.compstruct.2021.114420.

Nosier, A., and F. Fallah. 2009. Non-linear analysis of functionally graded circular plates under asymmetric transverse loading. *International Journal of Non-Linear Mechanics* 44: 928–942. doi: 10.1016/j.ijnonlinmec.2009.07.001.

Sun, C. T., and H. Chin. 1988. Analysis of asymmetric composite laminates. *AIAA Journal* 26: 714 –718. doi: 10.2514/3.9957.